



The g-C₃N₄ modified by AgBr and ZIF-8 adsorption-photocatalysis synergistic degradation of bisphenol A

Wei Zheng¹ · Sheng Feng¹ · Shanshan Feng¹ · Cong Shao¹ · Zhenfei Jiang¹ · Wei Wu¹ · Yunjie Ge¹ · Shenyu Liao¹ · Kunjie Li¹ · Chunying Duan² · Qi Meng³

Received: 9 September 2020 / Accepted: 11 December 2020 / Published online: 5 January 2021
© The Author(s), under exclusive licence to Springer Nature B.V. part of Springer Nature 2021

Abstract

In this work, a ternary complex (g-C₃N₄/ZIF-8/AgBr) was prepared by modifying the surface of the protonated graphitic carbon nitride (g-C₃N₄) with photosensitive AgBr and zeolitic imidazolate framework-8 (ZIF-8), and its physicochemical parameters, crystal morphology and electrochemical properties were characterized using a series of techniques. The modified g-C₃N₄ not only improves the ability to capture pollutants in water, but also efficiently catalyzes the degradation of bisphenol A (BPA) in water by rapidly producing superoxide radicals (O₂⁻), cavitation (h⁺) and hydroxyl radicals (OH) in visible light, with the removal efficiency reaching 80.4%. The activity of catalytic degradation of BPA from strong to weak is g-C₃N₄/ZIF-8/AgBr, g-C₃N₄/AgBr, g-C₃N₄/ZIF-8, AgBr, g-C₃N₄, ZIF-8. After four cycles of experiments, it was found that g-C₃N₄/ZIF-8/AgBr had still considerable degradation ability (70.2%) and stability.

Keywords g-C₃N₄/ZIF-8/AgBr · Photodegradation · Bisphenol A · Catalytic mechanism

Introduction

Photocatalytic degradation of pollutants by semiconductor is a new type of high-efficiency and energy-saving oxidation technology [1]. Among many photocatalytic materials, graphite carbon nitride (g-C₃N₄), as a metal-free polymer semiconductor composed of carbon and nitrogen elements, is easy to synthesize and

Supplementary Information The online version contains supplementary material available at <https://doi.org/10.1007/s11164-020-04360-z>.

✉ Sheng Feng
shfeng@cczu.edu.cn

Extended author information available on the last page of the article

low in cost [2–7]. It is widely used in the removal of environmental pollutants [3, 5, 8], water decomposition to produce hydrogen [9], carbon dioxide reduction [10] and selective photocatalytic reactions [11]. The g-C₃N₄ prepared and treated by ultrasonic irradiation under strong acid conditions has good photocatalytic activity [12]. However, the high recombination rate of photo-generated electron–hole pairs [13] of g-C₃N₄ always limits its catalytic efficiency. Up to now, a lot of research work has been used to improve the performance of g-C₃N₄, such as doping of precious metal [3, 10] and building heterostructures with other semiconductors [14].

Metal–organic frameworks (MOFs) are a new type of porous networks formed by linking organic ligands to metal ions [15–19]. In the MOFs family, zeolitic imidazolate framework-8 (ZIF-8) has most of the properties of MOFs materials [1, 20]. Due to its high specific surface area [21], chemical stability [22] and photocatalytic properties [14], it has been widely used as a porous adsorbent for adsorbing pollutants in water. Another feature of ZIF-8 is transparency [23], which makes it not only does not weaken the light absorption but also improve the efficiency of charge separation when combined with semiconductors, such as Bi₂S₃/ZIF-8 [15], MoO₃@ZIF-8 [17], TiO₂/ZIF-8 [20]. In order to enhance the adsorption performance of g-C₃N₄, ZIF-8 was assembled on its surface, which overcomes the shortcoming of a single component and improves the capture ability of pollutants. In addition, electron multiple transfer can be achieved by doping AgBr. It has been extensively studied as a photosensitive material in combination with semiconductors [24–26]. The surface plasma resonance (SPR) effect transfers the plasma electron from Ag to the conduction band (CB) of the semiconductor, which can effectively inhibit the recombination of electron–hole pairs to improve the photocatalytic activity of the catalyst [25, 27–29].

Based on the above analysis, a novel ternary photocatalytic material (g-C₃N₄/ZIF-8/AgBr) was synthesized by loading ZIF-8 and AgBr onto the surface of protonated g-C₃N₄ by the sonication-assisted deposition–precipitation method. In the experiment of photocatalytic degradation of bisphenol A (BPA), g-C₃N₄/ZIF-8/AgBr showed strong photocatalytic activity compared with other materials (text S1). Also, the reusability of ternary materials and the photocatalytic mechanism of pollutants degradation were analyzed.

Experimental

Materials

All chemicals used in the experiment were analytical grade, including melamine, 2-methylimidazole (2-MeIm), zinc nitrate hexahydrate (Zn(NO₃)₂·6H₂O), sulfuric acid (H₂SO₄), methanol (CH₃OH), ethanol (C₂H₅OH), sodium bromide (NaBr) and silver nitrate (AgNO₃), which were purchased from Aladdin Industrial Company. The water used in the synthesis of the sample was deionized water.

Synthesis of materials

g-C₃N₄

According to the reported method [30], an appropriate amount of melamine was put into an alumina crucible with a lid, which was heated in a muffle furnace for 4 h (550 °C, 5 °C/min). All experiments were performed in the air. Then, a yellow product (g-C₃N₄) was obtained. And g-C₃N₄ (0.1 g) was added to H₂SO₄ (80 mL), which was stirred and sonicated. Finally, g-C₃N₄ collected by centrifugation was washed with deionized water and dried at 60 °C for 24 h.

ZIF-8

Zn(NO₃)₂·6H₂O (10 mmol) and 2-MeIm (80 mmol) were added to CH₃OH, respectively [31]. Then, the solution was stirred vigorously at room temperature for 1 h. Finally, ZIF-8 was separated by centrifugation, washed several times with CH₃OH and deionized water and dried for 24 h at 80 °C.

g-C₃N₄/ZIF-8 and g-C₃N₄/ZIF-8/AgBr

Appropriate amounts of g-C₃N₄ were dissolved in deionized water and treated with ultrasound (40 kHz) for 1 h to obtain a solution (A). Zn(NO₃)₂·6H₂O was dissolved in CH₃OH to obtain a solution (B). 2-MeIm was dissolved in CH₃OH to obtain a solution (C). Next, B was added to A and the mixture was further treated with ultrasound (40 kHz) for 30 min. After that, C was added to the mixture above and stirred at room temperature for 2 h. After the reaction, g-C₃N₄/ZIF-8 was collected by centrifugation, washed three times and dried at 80 °C for 12 h.

g-C₃N₄/ZIF-8 was dissolved in deionized water and treated by ultrasound (40 kHz) for 30 min. With stirring, an appropriate amount of AgNO₃ solution and NaBr solution were added to the above mixture in turn and stirred at room temperature for 3 h. Finally, g-C₃N₄/ZIF-8/AgBr was collected by centrifugation, washed several times and dried at 70 °C for 12 h. The process is shown schematically in Fig. 1.

Characterization

Details of instruments used for characterization are in the supplementary material (text S2).

Photocatalytic experiments

Before the photocatalytic experiments, a standard solution of BPA (1 g/L) was prepared with CH₃OH as a solvent and then diluted to 10 mg/L with deionized water. At room temperature, 10 mg catalyst was added to 50 mL BPA solution

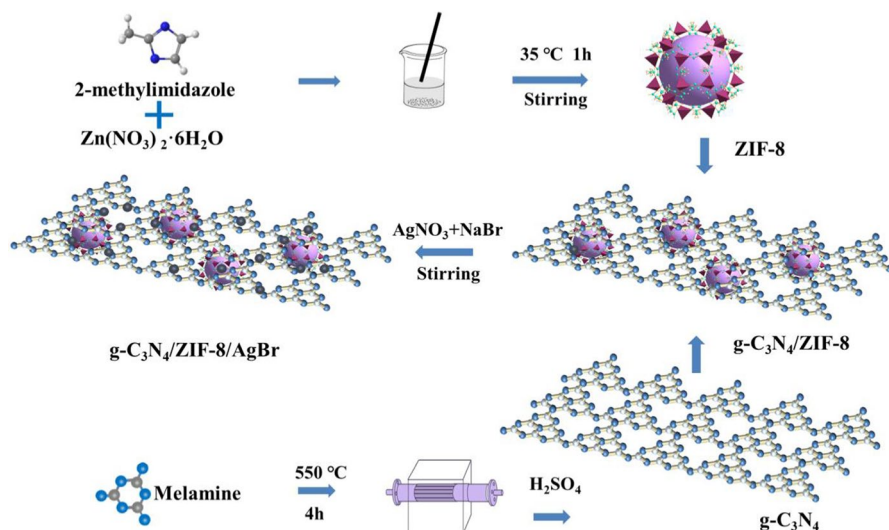


Fig. 1 Schematic illustration of the catalytic materials

($C_0 = 10 \text{ mg/L}$), which were stirred for 1 h under dark conditions to ensure the equilibrium of adsorption and desorption. Next, photocatalytic reactions were continued for 2 h under a 300 W xenon lamp and a small amount of solution was periodically taken. The photocatalysts in the solution were separated by the filter membrane. The concentration of BPA solution was determined by high-performance liquid chromatography (HPLC, LC-20AD, Shimadzu, Japan).

Results and discussion

Characterizations

Figure 2a shows X-ray diffraction (XRD) patterns of materials. $\text{g-C}_3\text{N}_4$ (JCPDS Card No. 87–1526) [3, 32] exhibited two characteristic peaks at 2θ values of 13.1° and 27.5° , respectively. The strong diffraction peak at 27.5° was attributed to the in-plane stacking of conjugated aromatic systems, corresponding to the (002) plane of $\text{g-C}_3\text{N}_4$. A small diffraction peak appears at 13.0° corresponds to (100) crystal planes related to the tri-s-triazine building units. Meanwhile, the diffraction peaks of ZIF-8 at 7.32° (011), 10.37° (002), 12.76° (112), 14.70° (022), 16.44° (013), 17.93° (222), 22.13° and 24.46° (233). The characterization results of $\text{g-C}_3\text{N}_4$ and ZIF-8 were consistent with the results of published literature [2, 9, 31, 33]. The diffraction peaks of AgBr (JCPDS Card No. 06–0438) at 26.68° (111), 30.99° (200), 44.30° (220), 54.97° (222), 64.40° (222) and 73.30° (420) [24, 34]. All characteristic peaks corresponding to $\text{g-C}_3\text{N}_4$ and AgBr were found on the XRD pattern of $\text{g-C}_3\text{N}_4/\text{ZIF-8}/\text{AgBr}$ and there were no other peaks. There were no obvious ZIF-8 peaks that could be detected in $\text{g-C}_3\text{N}_4/\text{ZIF-8}$ and $\text{g-C}_3\text{N}_4/\text{ZIF-8}/\text{AgBr}$ composites due to the

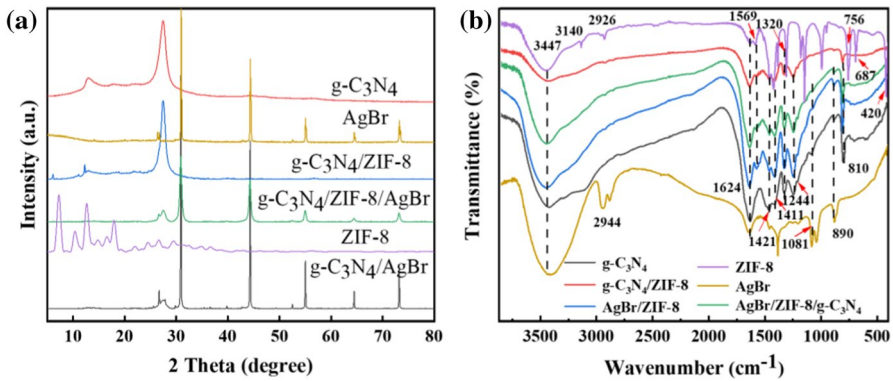


Fig. 2 XRD patterns (a) and FTIR spectra (b) of the catalytic materials

low content of ZIF-8. However, the two diffraction peaks corresponding to (100) and (002) of g-C₃N₄ in the composite material were relatively weak, which was caused by the strong electrostatic interaction between ZIF-8 nanoparticles and g-C₃N₄ [35]. This indicated that the g-C₃N₄ sheet were well-coupled with ZIF-8 and AgBr.

Functional group structures of materials were analyzed by Fourier transform infrared (FTIR) (Fig. 2b). The peaks of ZIF-8 at 3447 cm⁻¹, 3140 cm⁻¹ and 2926 cm⁻¹ were caused by the stretching vibration of N–H, imidazole aromatic and C–H in the imidazole ring, respectively. The peaks in the range of 900~1350 cm⁻¹ were formed by the in-plane bending of the pyridine ring. The characteristic peak less than 800 cm⁻¹ was attributed to the out-of-plane bending vibration of pyridine ring. The strong absorption band at 420 cm⁻¹ was attributed to the stretching vibration of the Zn–N bond [36]. g-C₃N₄ has characteristic peaks at 3000~3500 cm⁻¹, which were derived from the tensile vibration of N–H. The absorption peaks at 1624 cm⁻¹, 1569 cm⁻¹, 1457 cm⁻¹ and 1407 cm⁻¹ were due to the C=N and C–N tensile vibration. The absorption peaks around 1320 cm⁻¹ and 1244 cm⁻¹ were attributed to the vibration of C–N–C. And the characteristic peaks near 810 cm⁻¹ and 890 cm⁻¹ were caused by the bending and stretching vibration of the triazine ring. The characteristic peaks of monomers could be observed in the composite material, which indicated that the typical functional group structure of several monomers was not destroyed after the composite material was formed. However, the loading of ZIF-8 in the composite material was relatively small, which significantly weakened its characteristic peaks. In short, consistent with the XRD results, it was true that ZIF-8, g-C₃N₄ and AgBr were present in the composite material.

Figure 3 were the scanning electron microscope (SEM) results of the prepared catalyst. By observing the surface of g-C₃N₄ modified by ZIF-8 and AgBr, it was further confirmed that the composite material was successfully prepared. ZIF-8 had a regular dodecahedral structure with an average particle size of 70 nm (Fig. 3a) [37]. Protonated g-C₃N₄, as described in related literature [38], presented a sheet-like structure with a rough surface (Fig. 3b). Figure 3c shows the SEM results of g-C₃N₄/ZIF-8/AgBr and it could be seen that ZIF-8 and AgBr particles had been attached to the surface and clearance of g-C₃N₄ and their distribution was relatively

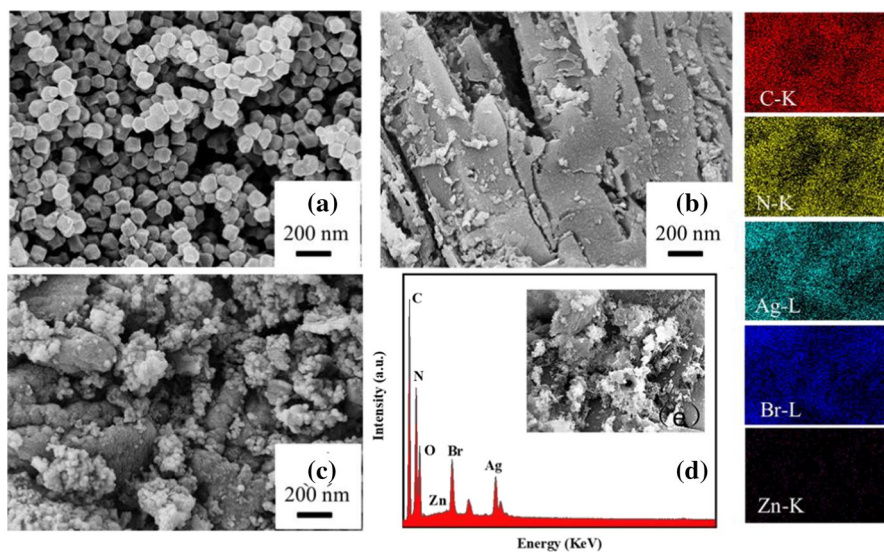


Fig. 3 SEM images of ZIF-8 (a), $g\text{-C}_3\text{N}_4$ (b) and $g\text{-C}_3\text{N}_4/\text{ZIF-8}/\text{AgBr}$ (c); FESEM-EDS figure (d) and Mapping (e) of $g\text{-C}_3\text{N}_4/\text{ZIF-8}/\text{AgBr}$

dispersed. EDS analysis was performed on the ternary material to further verify the presence of ZIF-8 and AgBr on the surface of $g\text{-C}_3\text{N}_4$ (Fig. 3d). The $g\text{-C}_3\text{N}_4/\text{ZIF-8}/\text{AgBr}$ contained C, N, Zn, Br and Ag elements, which were uniformly distributed according to the result of element mapping (Fig. 3e). In summary, ZIF-8 and AgBr particles were successfully loaded on the surface of $g\text{-C}_3\text{N}_4$.

The surface morphologies of the $g\text{-C}_3\text{N}_4/\text{ZIF-8}/\text{AgBr}$ was evaluated through transmission electron microscopy (TEM) and high-resolution transmission electron microscopy (HRTEM), and the results are exhibited in Fig. 4. As shown in Fig. 4a and b, the protonated $g\text{-C}_3\text{N}_4$ showed an irregular translucent sheet structure, which could provide a good platform for the in situ growth of ZIF-8 and AgBr. Some black particles were dispersed on the layered structure of $g\text{-C}_3\text{N}_4$, which was a result of the introduction of ZIF-8 and AgBr. ZIF-8 had a larger inner diameter and AgBr had a smaller inner diameter. Figure 4c shows the HRTEM diagram of ternary material, it could be seen that the lattice fringe of the AgBr with a spacing of 0.282 nm

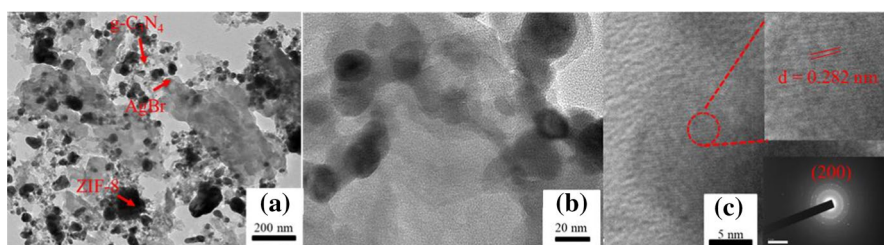


Fig. 4 TEM images of representative sample of $g\text{-C}_3\text{N}_4/\text{ZIF-8}/\text{AgBr}$ (a~c)

corresponded to the (200) surface. The selected electron diffraction pattern (SAED) further indicated that there was a diffusion ring corresponding to the (200) surface of AgBr. However, the results of TEM combined with the results of SEM and EDS showed that the ternary composite was successfully prepared.

The brunauer–emmett–teller (BET) surface area and pore structure of materials were characterized by N₂ adsorption–desorption measurements (text S3).

X-ray photoelectron spectroscopy (XPS) was used to further verify the chemical composition and bonding status of g-C₃N₄/ZIF-8/AgBr. In the full-spectrum XPS scan of g-C₃N₄/ZIF-8/AgBr (Fig. 5a), it was Ag, Br, C, N and Zn elements that could be observed. Figure 5b shows Ag 3d high-resolution XPS spectra of g-C₃N₄/ZIF-8/AgBr. The peaks of Ag 3d_{5/2} and Ag 3d_{3/2} were located at 367.3 eV and 373.3 eV, respectively, which were mainly attributed to Ag⁺. For the Br 3d spectra of g-C₃N₄/ZIF-8/AgBr shown in Fig. 5c, it could be seen that two peaks of Br 3d_{5/2} and Br 3d_{3/2} at binding energies of 67.8 eV and 68.9 eV. The two peaks were attributed to the presence of Br⁻ in the sample. The high-resolution XPS spectra of Zn 2p are shown in Fig. 5d. The two peaks at binding energy of 1021.6 eV and 1044.8 eV in g-C₃N₄/ZIF-8/AgBr ascribed to Zn 2p_{3/2} and Zn 2p_{1/2}, respectively. The N 1s high-resolution XPS spectrum could fit three peaks (Fig. 5e). Figure 5e shows the N 1s spectrum of g-C₃N₄/ZIF-8/AgBr, with three peaks at binding energy of 398.3 eV, 399.4 and 400.4 eV. The peak located at 398.3 eV was derived from sp² hybridized aromatic nitrogen atoms bound to carbon atoms (C=N–C). The peak at 399.4 eV could be ascribed to the N–(C)₃ bond formed by the connection of N atom and carbon atoms. The peak at around 400.4 eV represented the N–H bond. The C 1s high-resolution XPS spectrum of g-C₃N₄/ZIF-8/AgBr shown in Fig. 5f, two dominant peaks at 284.7 eV and 287.9 eV corresponded to C=C and N=C–N bonds, respectively. The XPS results further indicated that g-C₃N₄, ZIF-8 and AgBr co-existed in the composite.

It was necessary to analyze the photogenic electron–hole pairs recombination of material by photoluminescence (PL) spectra to detect the optical properties of the prepared photocatalytic materials. A material with a strong fluorescence signal had a higher electron–hole pairs recombination rate than a material with a weak fluorescence signal [34, 39]. As shown in Fig. 6, the PL intensity of ZIF-8 was the strongest among all samples, and the fluorescent signal of g-C₃N₄ was slightly weaker than that of ZIF-8. Compared with ZIF-8 and g-C₃N₄, AgBr showed the weakest fluorescence signal. However, the g-C₃N₄ modified by ZIF-8 and AgBr showed a quenched fluorescence signal. The fluorescence signal of g-C₃N₄/ZIF-8/AgBr was weaker than that of other materials, which reflected that the composite material had a higher photo-generated carrier separation efficiency.

The optical absorption characteristics of materials were analyzed by UV–vis diffuse reflectance spectroscopy (DRS) spectroscopy (Fig. 7a) and the band gap width was calculated (Fig. 7b).

As shown in Fig. 7a, g-C₃N₄ showed stronger absorbance in both UV and visible range [40, 41]. The absorption band edge of ZIF-8 was around 250 nm, which had good ultraviolet absorption capacity [17]. The absorption edge of AgBr was 550 nm, which was caused by Ag⁺ inevitably reduced to elemental Ag under irradiation [42]. Compared with g-C₃N₄, the absorption edge of g-C₃N₄/ZIF-8/AgBr was red-shifted to

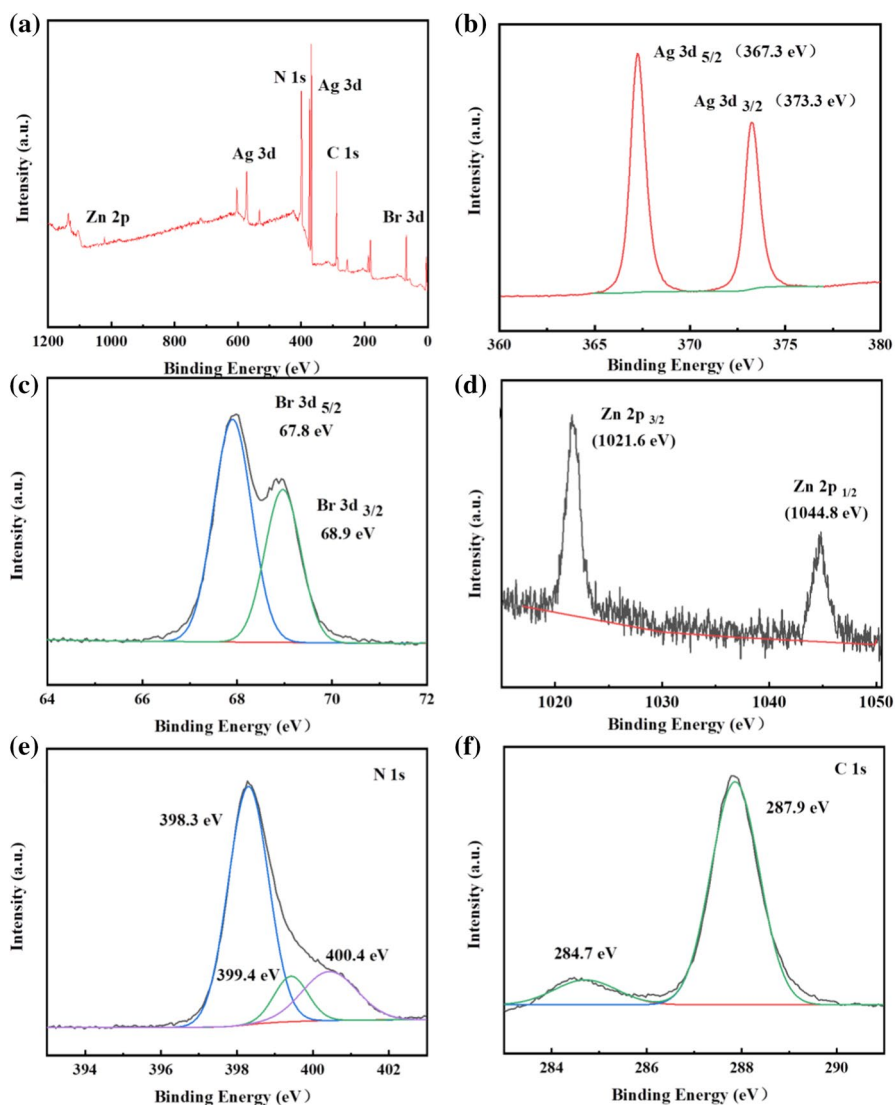


Fig. 5 XPS survey spectra of g-C₃N₄/ZIF-8/AgBr (a) and high-resolution XPS spectra of Ag 3d (b), Br 3d (c), Zn 2p (d), N 1s (e) and C 1s (f)

utilize more visible light. This might be due to the plasma resonance effect of AgBr on surface of g-C₃N₄. According to formula (1), the band gap width of the materials was calculated. Meanwhile, according to formula (2) and (3), the valence band (VB) and conduction band (CB) position of the materials were calculated [8, 43, 44].

$$(\alpha h\nu) = A(h\nu - E_g)^{1/n} \quad (1)$$

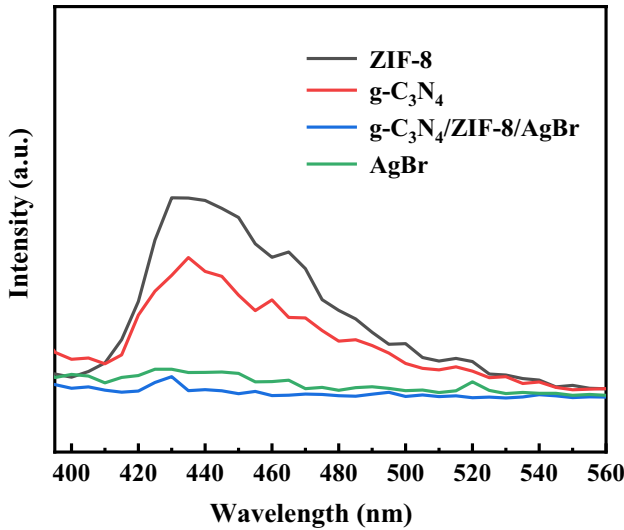


Fig. 6 Photoluminescence (PL) spectra of prepared materials

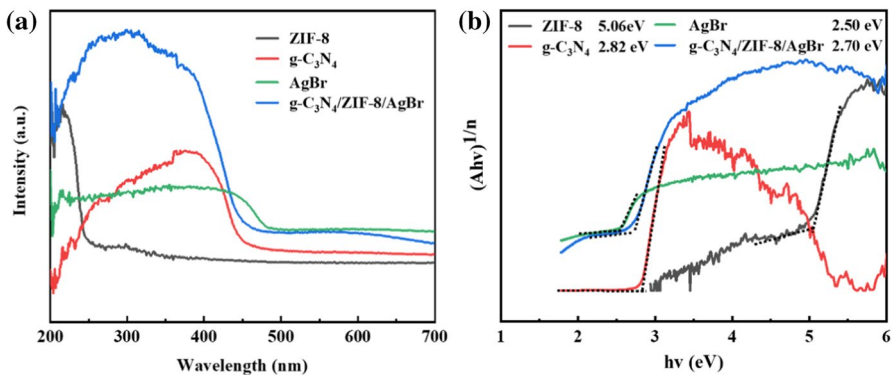


Fig. 7 UV-Vis DRS (a) and band gap (b) of ZIF-8, g-C₃N₄, AgBr and g-C₃N₄/ZIF-8/AgBr

$$E_{VB} = X - E^e + 0.5Eg \tag{2}$$

$$E_{CB} = E_{VB} - E_g \tag{3}$$

Among them, α , h , A and ν represented absorption coefficient, Planck constant, proportional constant and optical frequency, separately. For a direct transition, $n=2$; for indirect transition, $n=1/2$. E_g was the band gap energy of semiconductor. E_{CB} (E_{VB}), X and E^e represented the CB (VB) potential, electronegativity of compound and relative standard hydrogen electrode potential (4.5 eV), respectively.

The band gaps of ZIF-8, g-C₃N₄, AgBr and g-C₃N₄/ZIF-8/AgBr were 5.06, 2.82, 2.50 and 2.70 eV, respectively [17, 40–42]. The E_{CB} (E_{VB}) of ZIF-8, g-C₃N₄ and

AgBr were, respectively, -3.39 eV (1.67 eV), -1.24 eV (1.58 eV) and 0.07 eV (2.57 eV). It could be found that $g\text{-C}_3\text{N}_4$ and AgBr with a narrow band gap and ZIF-8 with a wide band gap could utilize visible and ultraviolet light, respectively. Therefore, it could be predicted that the energy utilization efficiency would be enhanced after the three materials were combined.

Analysis of the photocatalytic reactions

Adsorption experiments

10 mg of different materials were added to 50 mL BPA solution with concentrations of 2, 4, 6, 8 and 10 mg/L and the system was allowed to react for 1 h in the dark. As shown in Fig. 8a and b, the results of adsorption experiments under different concentrations of BPA in the dark. As a monomer material, it was obvious that ZIF-8 had the strongest adsorption performance, with an adsorption capacity (q_e) of 26.96 mg/g [45]. On the contrary, compared with ZIF-8, the adsorption capacity of AgBr (11.52 mg/g) and $g\text{-C}_3\text{N}_4$ (7.58 mg/g) was weaker. Compared with $g\text{-C}_3\text{N}_4$, it was found that the adsorption performance of ternary materials (The q_e of $g\text{-C}_3\text{N}_4/\text{ZIF-8}/\text{AgBr}$ was 12.93 mg/g) was better than that of binary materials (The q_e of $g\text{-C}_3\text{N}_4/\text{ZIF-8}$ and $g\text{-C}_3\text{N}_4/\text{AgBr}$ were 9.29 mg/g and 7.30 mg/g, respectively), which might be attributed to the doping of porous materials that provided more active sites for BPA. Langmuir adsorption isotherm model could be employed to understand the adsorption behaviors of BPA on the catalyst (text S4). As shown in Fig. 8c, the adsorption of different materials was well in line with the Langmuir isotherm and their maximum adsorption capacities were calculated to be 27.17 mg/g (ZIF-8), 14.42 mg/g (AgBr), 11.06 mg/g ($g\text{-C}_3\text{N}_4$), 7.92 mg/g ($g\text{-C}_3\text{N}_4/\text{AgBr}$), 14.05 mg/g ($g\text{-C}_3\text{N}_4/\text{ZIF-8}$) and 16.23 mg/g ($g\text{-C}_3\text{N}_4/\text{ZIF-8}/\text{AgBr}$), which meant that all materials could reach adsorption equilibrium in the dark for about 1 h.

Photocatalytic degradation of BPA

After stirring for 1 h in the dark, the photocatalytic reaction was carried out under the irradiation of a xenon lamp for 2 h and water samples were taken every 20 min. The experimental results are shown in Fig. 8d, ZIF-8 exhibited the strongest adsorption performance, but its photocatalytic performance under visible light was also the weakest, which exactly verified the results of UV-vis DRS. After 2 h of visible-light irradiation, only 31.8% and 21.6% of BPA were degraded by protonated $g\text{-C}_3\text{N}_4$ and AgBr, and their photocatalytic performance was average. On the contrary, the catalytic performance of binary materials had been improved slight. Compared with $g\text{-C}_3\text{N}_4$, $g\text{-C}_3\text{N}_4/\text{ZIF-8}$ and $g\text{-C}_3\text{N}_4/\text{AgBr}$ degraded 42.4% and 50.3% of BPA, respectively. Similarly, compared with $g\text{-C}_3\text{N}_4$, $g\text{-C}_3\text{N}_4/\text{ZIF-8}/\text{AgBr}$ had improved the adsorption and photocatalytic performance, and the removal of BPA was 80.4% during the entire reaction. The high photocatalytic performance of the $g\text{-C}_3\text{N}_4/\text{ZIF-8}/\text{AgBr}$ material was attributed to the effective inhibition of photo-generated electron-hole recombination after ZIF-8 and AgBr

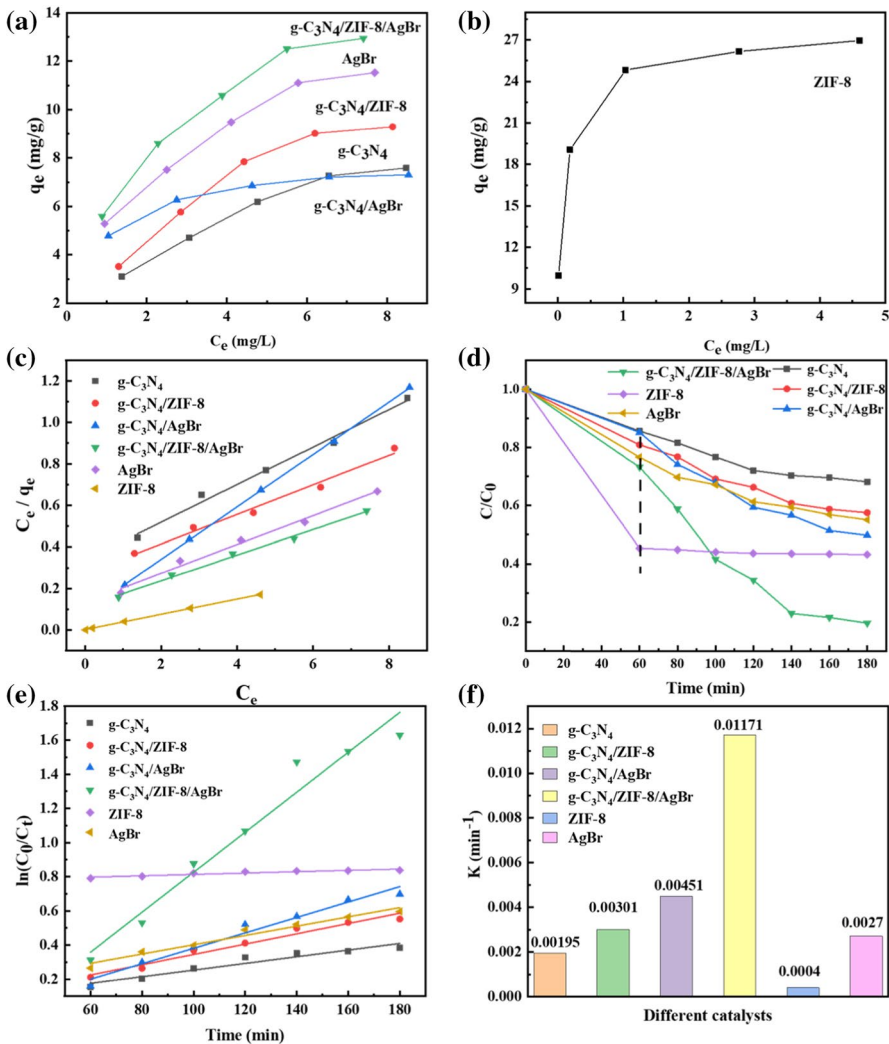


Fig. 8 Adsorption isotherm of different materials to BPA (a, b); Langmuir adsorption isotherm models of different materials (c); the effect of different materials on the degradation of BPA under visible light (d); corresponding to the pseudo-first-order kinetics of the degradation of BPA (e) and the reaction rate constants of different catalysts (f)

doping in the visible light region. The pseudo-first-order kinetic equation was used to describe the kinetics of the photocatalytic degradation of BPA (text S5). Figure 8e and f showed the kinetic fitting results of BPA degradation by different catalysts under visible light. Obviously, the results shown that the rate constant of g-C₃N₄/ZIF-8/AgBr ($k=0.01171 \text{ min}^{-1}$) was the highest, which was 6.0, 29.3, 4.3, 3.8 and 2.6 times that of g-C₃N₄ ($k=0.00195 \text{ min}^{-1}$), ZIF-8 ($k=0.00040 \text{ min}^{-1}$), AgBr ($K=0.00270 \text{ min}^{-1}$), g-C₃N₄/ZIF-8 ($k=0.00301 \text{ min}^{-1}$) and g-C₃N₄/AgBr

($k = 0.00451 \text{ min}^{-1}$), respectively. The catalytic efficiency of $\text{g-C}_3\text{N}_4/\text{ZIF-8}/\text{AgBr}$ was still considerable compared with similar catalysts (text S1). It could be seen that $\text{g-C}_3\text{N}_4$ modified by ZIF-8 and AgBr exhibited stronger adsorption capacity and photocatalytic activity.

Cyclic experiments

The recyclability and stability of $\text{g-C}_3\text{N}_4/\text{ZIF-8}/\text{AgBr}$ were explored by degrading BPA for four batches to degrade BPA solution (50 mg/L) under the same condition. As shown in Fig. 9a, the degradation efficiency dropped from 80.4% (the first time) to 70.2% (the fourth time), which was due to the loss of catalyst during the collection process. When $\text{g-C}_3\text{N}_4/\text{ZIF-8}/\text{AgBr}$ was exposed to visible light, the AgBr on the surface of $\text{g-C}_3\text{N}_4/\text{ZIF-8}/\text{AgBr}$ would be decomposed into Ag monomers, which could improve the photocatalytic degradation efficiency of $\text{g-C}_3\text{N}_4/\text{ZIF-8}/\text{AgBr}$ through SPR. However, Ag monomer loaded on the surface of AgBr could reduce its light absorption performance and the degradation efficiency showed a decreasing trend in the four-cycle experiment. The material after the cycle experiment was characterized by XRD. As shown in Fig. 9b, the peak of Ag monomer appeared at about 38° [42, 46], which was attributed to the decomposition of part of AgBr. It was loaded on the surface of AgBr and prevented the further decomposition of AgBr. From the XRD patterns, it could be clearly observed that the crystal structure of the material had not changed. The results of cyclic experiments and XRD proved that $\text{g-C}_3\text{N}_4/\text{ZIF-8}/\text{AgBr}$ had good reusability.

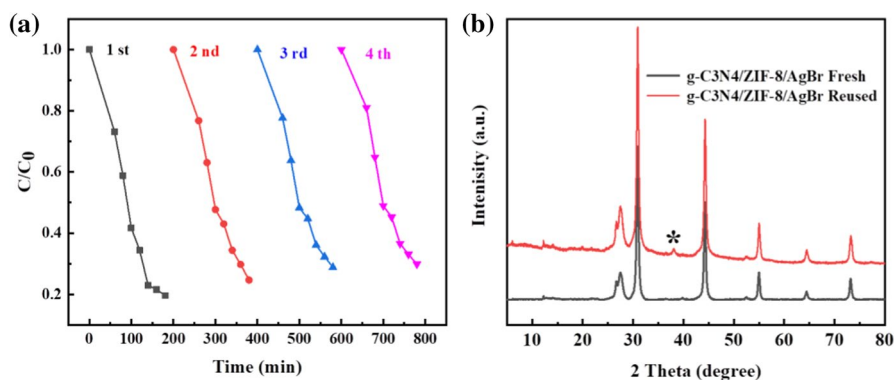


Fig. 9 Photocatalytic degradation of BPA by $\text{g-C}_3\text{N}_4/\text{ZIF-8}/\text{AgBr}$ four times (a); the XRD patterns of $\text{g-C}_3\text{N}_4/\text{ZIF-8}/\text{AgBr}$ (b)

Analysis of photocatalytic degradation of BPA

Free radical capture experiment

Active substance played an important role in the degradation of BPA. The free radical capture experiment was used to determine which active substance played the main role in the experiment of degradation of BPA. 1, 4-benzoquinone (BQ), isopropanol (IPA) and disodium edetate (EDTA-2Na) were usually added as scavenging agents for $\cdot\text{O}_2^-$, $\cdot\text{OH}$ and h^+ [8, 15, 47, 48]. In the presence of all scavengers, the efficiency of g-C₃N₄/ZIF-8/AgBr for catalyzing BPA was slightly reduced, which meant that $\cdot\text{O}_2^-$, $\cdot\text{OH}$ and h^+ were involved in the catalytic process. As shown in Fig. 10, the quenching effect of BQ was more obvious than the other two scavengers. The results showed that $\cdot\text{O}_2^-$ played a major role, h^+ played a smaller role and $\cdot\text{OH}$ played the weakest role in the reaction system. In addition, methanol as a carrier solvent was also a common hole scavenger and should be considered. When the methanol concentration was lower than 0.5 mol/L, BPA might also be degraded through the action of hydroxyl radicals [49, 50]. When methanol was used as a carrier solvent to dissolve BPA, the concentration of methanol could be changed to control its impact on the degradation of pollutants (text S6). It was undeniable that methanol affected the degradation effect of the material on BPA.

Photocatalytic mechanism

The main factor affecting the photocatalytic degradation of BPA was the rapid separation of photoelectrons–holes. The electron transport ability of ZIF-8, g-C₃N₄ and AgBr affected the efficiency of electron–hole separation. Based on

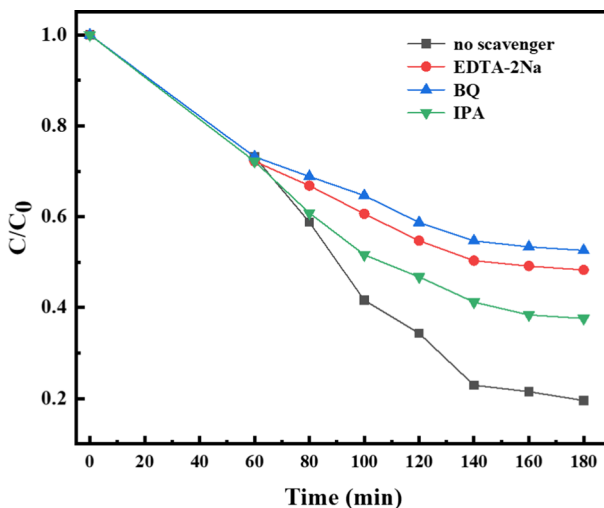


Fig. 10 Radical trapping experiment of g-C₃N₄/ZIF-8/AgBr catalytic degradation of BPA under visible light

the above characterization results and experimental conclusions, the catalytic degradation mechanism of BPA under visible light was proposed. As shown in Fig. 7, the CB (VB) of ZIF-8, $g\text{-C}_3\text{N}_4$ and AgBr were -3.39 eV (1.67 eV), -1.24 eV (1.58 eV) and 0.07 eV (2.57 eV), respectively. AgBr and $g\text{-C}_3\text{N}_4$ had visible light absorption capacity and could excite to produce electrons and holes under visible light irradiation. Since the E_g of ZIF-8 was 5.06 eV, it could not be excited under visible light irradiation. As shown in Fig. 11, after illumination, Ag decomposed from AgBr would act as an electronic bridge under SPR effect. The excited electrons were transitioned from the VB to CB of AgBr and $g\text{-C}_3\text{N}_4$ and part of the electrons in their CB flowed through Ag to ZIF-8. In the ternary material, multiple transfer paths of electron effectively suppressed the recombination of photo-generated electron–hole pairs and the utilization of photo-generated electrons was effectively improved. At the same time, combined with the analysis of capture experimental results, the other part of photo-generated electrons generated in CB of AgBr would recombine with $g\text{-C}_3\text{N}_4$. In addition, the electron potential of CB of $g\text{-C}_3\text{N}_4$ (-1.24 eV) was smaller than the potential of O_2/O_2^- (-0.043 eV), which could convert O_2 into $\cdot\text{O}_2^-$. The VB of AgBr ($+2.57$ eV) was greater than $\cdot\text{OH}/\text{H}_2\text{O}$ ($+1.99$ eV) [51–53], so the h^+ could oxidize H_2O to $\cdot\text{OH}$. After absorbing visible light, the composite material could produce $\cdot\text{O}_2^-$, h^+ and $\cdot\text{OH}$, which further degraded BPA.

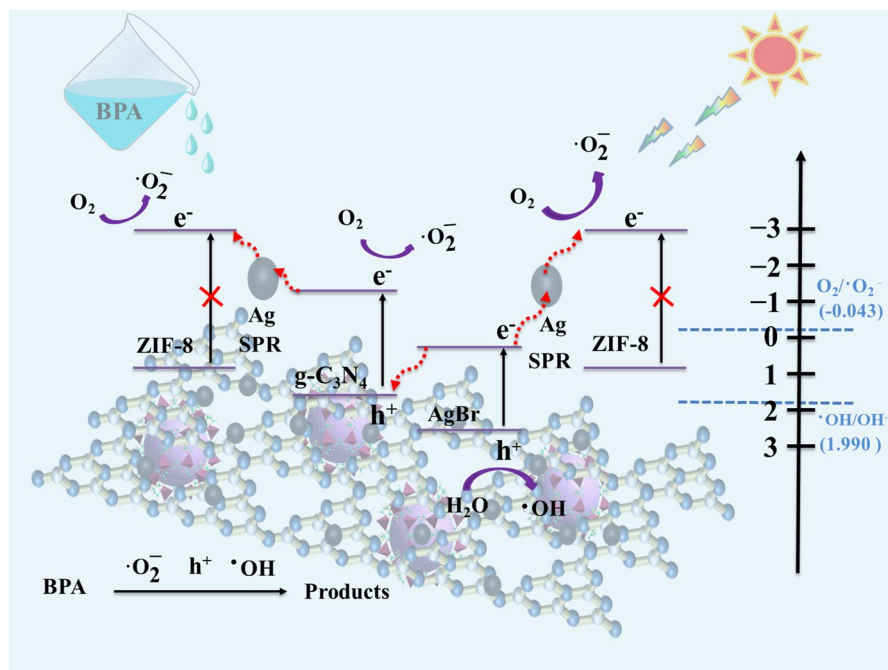


Fig. 11 Degradation mechanism of $g\text{-C}_3\text{N}_4/\text{ZIF-8}/\text{AgBr}$ on BPA

Conclusions

The ternary catalyst of g-C₃N₄ modified by AgBr and ZIF-8 was successfully prepared. The protonated g-C₃N₄ was the substrate, together with ZIF-8 and AgBr, a dual functional material of adsorption and catalysis was constructed. The g-C₃N₄/ZIF-8/AgBr improved the ability to capture BPA by providing more active sites. At the same time, multi-path electron transfer could effectively inhibit electron-hole recombination to improve the degradation efficiency of BPA and the reaction rate constants were 6.0, 29.3 and 4.3 times that of g-C₃N₄, ZIF-8 and AgBr, respectively. Free radical capture experiments showed that predominant active oxygen species for BPA degradation was identified to be the 'O₂⁻'. Cycle experiments showed that g-C₃N₄/ZIF-8/AgBr had excellent stability and reusability. Based on the above considerations, this work provided experience for the design and preparation of new materials for the synergistic degradation of BPA by adsorption and catalysis.

Acknowledgements The authors sincerely acknowledged financial supports from the National Natural Science Foundation of China (No. 41371446, 41271498 and 22075032); the Chinese National Funding of Social Sciences (No. 16BJL074); Natural science fund for colleges and universities in Jiangsu Province (18KJB610001); Natural Science Foundation of Jiangsu Province (BK20180964); Postgraduate Research & Practice Innovation Program of Jiangsu Province (No. KYCX20_2578 and SJCX20_0937).

Compliance with ethical standards

Conflict of interest The authors declare no competing interest.

References

1. J. Liu, R. Li, Y. Hu, T. Li, Z. Jia, Y. Wang, Y. Wang, X. Zhang, C. Fan, *Appl Catal B.* **202**, 64 (2017)
2. J. Zhou, W. Liu, W. Cai, *Sci. Total Environ.* **696**, 133962 (2019)
3. A. Akhundi, A. Habibi-Yangjeh, *Adv. Powder Technol.* **28**, 565 (2017)
4. Z. Zhao, Y. Sun, F. Dong, *Nanoscale* **7**, 15 (2015)
5. S. Hu, W. Ouyang, L. Guo, Z. Lin, X. Jiang, B. Qiu, G. Chen, *Biosens. Bioelectron.* **92**, 718 (2017)
6. M. Mousavi, A. Habibi-Yangjeh, M. Abitorabi, *J. Colloid Sci.* **480**, 218 (2016)
7. J. Wen, J. Xie, X. Chen, X. Li, *Appl. Surf. Sci.* **391**, 72 (2017)
8. S. Kumar, S. T. B. Kumar, A. Baruah and V. Shanker, *J. Phys. Chem. C*, **117**, 26135 (2013)
9. Z.-A. Lan, G. Zhang, X. Wang, *Appl. Catal B.* **192**, 116 (2016)
10. W.-J. Ong, L.K. Putri, L.-L. Tan, S.-P. Chai, S.-T. Yong, *Appl. Catal B.* **180**, 530 (2016)
11. G. Marci, E.I. García-López, L. Palmisano, *Catal. Today* **315**, 126 (2018)
12. A. Akhundi, E.I. García-López, G. Marci, A. Habibi-Yangjeh, L. Palmisano, *Res. Chem. Intermed.* **43**, 5153 (2017)
13. W.-D. Oh, L.-W. Lok, A. Veksha, A. Giannis, T.-T. Lim, *Chem. Eng. J.* **333**, 739 (2018)
14. X. Liu, J. Zhang, Y. Dong, H. Li, Y. Xia, H. Wang, *New J. Chem.* **42**, 12180 (2018)
15. Y.H. Ding, X.L. Zhang, N. Zhang, J.Y. Zhang, R. Zhang, Y.F. Liu and Y.Z. Fang *Dalton* (2018) *Trans.* **47**; 684
16. M. Jiang, X. Cao, D. Zhu, Y. Duan, J. Zhang, *Electrochim. Acta* **196**, 699 (2016)
17. Y. Zhang, S.-J. Park, *Appl. Catal B.* **240**, 92 (2019)
18. Q. Liang, S. Cui, J. Jin, C. Liu, S. Xu, C. Yao, Z. Li, *Appl. Surf. Sci.* **456**, 899 (2018)
19. W. Huang, N. Liu, X. Zhang, M. Wu, L. Tang, *Appl. Surf. Sci.* **425**, 107 (2017)
20. X. Zeng, L. Huang, C. Wang, J. Wang, J. Li, X. Luo, *A.C.S. Appl. Mater. Interfaces* **8**, 20274 (2016)

21. D. Fairen-Jimenez, S. Moggach, M. Wharmby, P. Wright, S. Parsons, T. Düren, *J. Am. Chem. Soc.* **133**, 8900 (2011)
22. W. Zhou, B. Zou, W. Zhang, D. Tian, W. Huang, F. Huo, *Nanoscale* **7**, 8720 (2015)
23. S. Liu, J. Wang, J. Yu, *RSC Adv.* **6**, 59998 (2016)
24. Y. He, L. Zeng, Z. Feng, Q. Zhang, X. Zhao, S. Ge, X. Hu, H. Lin, *Adv. Powder Technol.* **31**, 439 (2020)
25. M. Xie, D. Wang, L. Jing, W. Wei, Y. Xu, H. Xu, H. Li, J. Xie, *Appl. Surf. Sci.* **521**, 146343 (2020)
26. X. Wang, S. Yuan, S. Chen, G. Chen, J. Zhang, L. Zhang, *Res. Chem. Intermed.* **41**, 5137 (2014)
27. R. Wang, J. Tang, X. Zhang, D. Wang, X. Wang, S. Xue, Z. Zhang, D.D. Dionysiou, *J. Hazard. Mater.* **375**, 161 (2019)
28. Y. Zeng, N. Guo, H. Li, Q. Wang, X. Xu, Y. Yu, X. Han, H. Yu, *Sci. Total Environ.* **659**, 20 (2019)
29. A. Kumar, S.K. Sharma, G. Sharma, A.a.H. Al-Muhtaseb, M. Naushad, A.A. Ghfar and F.J. Stadler (2019) *J Hazard Mater.* **364**; 429
30. Y. Gong, X. Zhao, H. Zhang, B. Yang, K. Xiao, T. Guo, J. Zhang, H. Shao, Y. Wang, G. Yu, *Appl. Catal B.* **233**, 35 (2018)
31. G. Fan, X. Zheng, J. Luo, H. Peng, H. Lin, M. Bao, L. Hong, J. Zhou, *Chem. Eng. J.* **351**, 782 (2018)
32. N. Tian, H. Huang, S. Wang, T. Zhang, X. Du, Y. Zhang, *Appl. Catal B.* **267**, 118697 (2020)
33. A. Kumar, G. Sharma, M. Naushad, A.H. Al-Muhtaseb, A. Kumar, I. Hira, T. Ahamad, A.A. Ghfar, F.J. Stadler, *J. Environ. Manage.* **231**, 1164 (2019)
34. Y. Zhang, Z.-R. Tang, X. Fu, Y.-J. Xu, *Appl. Catal B.* **106**, 445 (2011)
35. D. Yuan, J. Ding, J. Zhou, L. Wang, H. Wan, W.-L. Dai, G. Guan, *J. Alloys Compd.* **762**, 98 (2018)
36. M.J.C. Ordoñez, K.J. Balkus, J.P. Ferraris, I.H. Musselman, *J. Membr. Sci.* **361**, 28 (2010)
37. J.J. Beh, J.K. Lim, E.P. Ng, B.S. Ooi, *Mater. Chem. Phys.* **216**, 393 (2018)
38. H. Zhang, G. Tang, X. Wan, J. Xu, H. Tang, *Appl. Surf. Sci.* **530**, 147234 (2020)
39. L. Ge, C. Han, J. Liu, *Appl. Catal B.* **108–109**, 100 (2011)
40. T. Li, L. Zhao, Y. He, J. Cai, M. Luo, J. Lin, *Appl. Catal B.* **129**, 255 (2013)
41. Y. Yang, W. Guo, Y. Guo, Y. Zhao, X. Yuan, Y. Guo, *J. Hazard. Mater.* **271**, 150 (2014)
42. F. Chen, W. An, L. Liu, Y. Liang, W. Cui, *Appl. Catal B.* **217**, 65 (2017)
43. N. Serpone, D. Lawless, R. Khairutdinov, *J. Phys. Chem.* **99**, 16646 (1995)
44. J. Cao, B. Luo, H. Lin, B. Xu, S. Chen, *J. Hazard. Mater.* **217–218**, 107 (2012)
45. J. Peng, X. Sun, Y. Li, C. Huang, J. Jin, Dhanjai, J. Wang and J. Chen, *Microporous Mesoporous Mater.*, **268**, 268
46. P. Wang, B. Huang, X. Qin, X. Zhang, Y. Dai, M.-H. Whangbo, *Inorg. Chem.* **48**, 10697 (2009)
47. Q. Zhu, Y. Sun, F. Na, J. Wei, S. Xu, Y. Li, F. Guo, *Appl. Catal B.* **254**, 541 (2019)
48. Y. Yang, J. Wu, T. Xiao, Z. Tang, J. Shen, H. Li, Y. Zhou, Z. Zou, *Appl. Catal B.* **255**, 117771 (2019)
49. M.J. Arlos, R. Liang, L.C.M. Li Chun Fong, N.Y. Zhou, C.J. Ptacek, S.A. Andrews and M.R. Servos (2017) *J. Environ. Chem. Eng.* **5**; 4497
50. L. Sun, J.R. Bolton, *J. Phys. Chem.* **100**, 4127 (1996)
51. H.-J. Hou, X.-H. Zhang, D.-K. Huang, X. Ding, S.-Y. Wang, X.-L. Yang, S.-Q. Li, Y.-G. Xiang and H. Chen, *Appl. Catal., B.* **203**, 563 (2017)
52. J. Yue, M. Yuan, X. Zhang, G. Wen, G. Ren, B. Ge, L. Zhao and X. Shao *Colloids Surf., A*, **601**, 124992 (2020)
53. A. Kumar, A. Rana, G. Sharma, M. Naushad, A.H. Al-Muhtaseb, C. Guo, A. Iglesias-Juez, F.J. Stadler, *A.C.S. Appl. Mater. Interfaces* **10**, 40474 (2018)

Publisher's Note Springer Nature remains neutral with regard to jurisdictional claims in published maps and institutional affiliations.

Affiliations

Wei Zheng¹ · Sheng Feng¹ · Shanshan Feng¹ · Cong Shao¹ · Zhenfei Jiang¹ · Wei Wu¹ · Yunjie Ge¹ · Shenyu Liao¹ · Kunjie Li¹ · Chunying Duan² · Qi Meng³

Wei Zheng
ZW17862930738@163.com

Shanshan Feng
fss728@163.com

Cong Shao
CongShaoCCZU@outlook.com

Zhenfei Jiang
15706140775@163.com

Wei Wu
1564611063@qq.com

Yunjie Ge
3115905489@qq.com

Shenyu Liao
16381897420@qq.com

Kunjie Li
799862443@qq.com

Chunying Duan
cyduan@dlut.edu.cn

Qi Meng
mengqi@cczu.edu.cn

¹ School of Environmental and Safety Engineering, Changzhou University, Jiangsu 213164, China

² Department of Chemical and Environmental Life Sciences, Dalian University of Technology, Dalian 116024, China

³ School of Petroleum Engineering, Changzhou University, Jiangsu 213164, China